Computers in Biology and Medicine 105 (2019) 112–124

Contents lists available at ScienceDirect

Computers in Biology and Medicine

journal homepage: www.elsevier.com/locate/compbiomed

Deep structure tensor graph search framework for automated extraction and characterization of retinal layers and fluid pathology in retinal SD-OCT scans

Taimur Hassan[a,b,*], Muhammad Usman Akram[a], Muhammad Furqan Masood[c], Ubaidullah Yasin[d]

[a] Department of Computer and Software Engineering, National University of Sciences and Technology (NUST), Islamabad, Pakistan
[b] Department of Electrical Engineering, Bahria University, Islamabad, Pakistan
[c] Department of Electrical and Computer Engineering, Center for Advanced Studies in Engineering (CASE), Islamabad, Pakistan
[d] Department of Ophthalmology, Armed Forces Institute of Ophthalmology (AFIO), Rawalpindi, Pakistan

ARTICLE INFO

Keywords:
Optical coherence tomography (OCT)
Ophthalmology
Maculopathy
Convolutional neural network (CNN)
Graph search

ABSTRACT

Maculopathy is a group of retinal disorders that affect macula and cause severe visual impairment if not treated in time. Many computer-aided diagnostic methods have been proposed over the past that automatically detect macular diseases. However, to our best knowledge, no literature is available that provides an end-to-end solution for analyzing healthy and diseased macular pathology. This paper proposes a vendor-independent deep convolutional neural network and structure tensor graph search-based segmentation framework (CNN-STGS) for the extraction and characterization of retinal layers and fluid pathology, along with 3-D retinal profiling. CNN-STGS works by first extracting nine layers from an optical coherence tomography (OCT) scan. Afterward, the extracted layers, combined with a deep CNN model, are used to automatically segment cyst and serous pathology, followed by the autonomous 3-D retinal profiling. CNN-STGS has been validated on publicly available Duke datasets (containing a cumulative of 42,281 scans from 439 subjects) and Armed Forces Institute of Ophthalmology dataset (containing 4260 OCT scans of 51 subjects), which are acquired through different OCT machinery. The performance of the CNN-STGS framework is validated through the marked annotations, and it significantly outperforms the existing solutions in various metrics. The proposed CNN-STGS framework achieved a mean Dice coefficient of 0.906 for segmenting retinal fluids, along with an accuracy of 98.75% for characterizing cyst and serous fluid from diseased retinal OCT scans.

1. Introduction

Sight is an important sense for human beings [1]. The human eye mainly consists of three layers [2]. The outer layer is called sclera, which protects the eyeball from the external environment. Beneath sclera lies the choroid, which contains blood vessels and provides nourishment to the eyeball. The retina is the innermost layer of the eye that is responsible for vision formation [2]. It is divided into two major parts, the macula and the peripheral retina. The macula is responsible for discriminating vision intensity and color information, and it has a diameter of 5500 microns. The retinal region outside the macula is known as the peripheral retina, which is responsible for side vision. The image formed on the retina goes to the brain for interpretation via the optic nerve [2] situated within the blind spot region. Macular disorders damage the macula, which results in vision loss and even blindness. Macular edema (ME), also known as retinal edema, is one of the most common macular syndromes. It is often associated with diabetes, and in that case, it is termed as “diabetic macular edema” (DME). Occasionally, ME also occurs because of cataract surgeries and therefore referred to as cystoid macular edema (CME) due to the cyst formation within retinal layers [3]. Central serous retinopathy (CSR), commonly found in young people, occurs because of the increased hydrostatic pressure in the choroid that produces serous fluid beneath the neurosensory retina [4]. Age-related macular degeneration (AMD) is another macular syndrome that is mostly found in elderly people because of smoking, alcohol, or through family genes. Although AMD alone does not lead toward blindness, it causes significant vision loss. Maculopathy can be detected through various techniques such as fluorescein angiography (FA), fundus photography (FP) [5], and optical coherence tomography (OCT). OCT imaging is a recently introduced eye testing method that can be used for evaluating early retinopathy cases. OCT images are acquired noninvasively, and they provide an objective visualization of

* Corresponding author. Department of Computer and Software Engineering, National University of Sciences and Technology (NUST), Islamabad, Pakistan.
E-mail address: engr.taimoorhassan@gmail.com (T. Hassan).

https://doi.org/10.1016/j.compbiomed.2018.12.015
Received 4 July 2018; Received in revised form 25 December 2018; Accepted 29 December 2018
0010-4825/

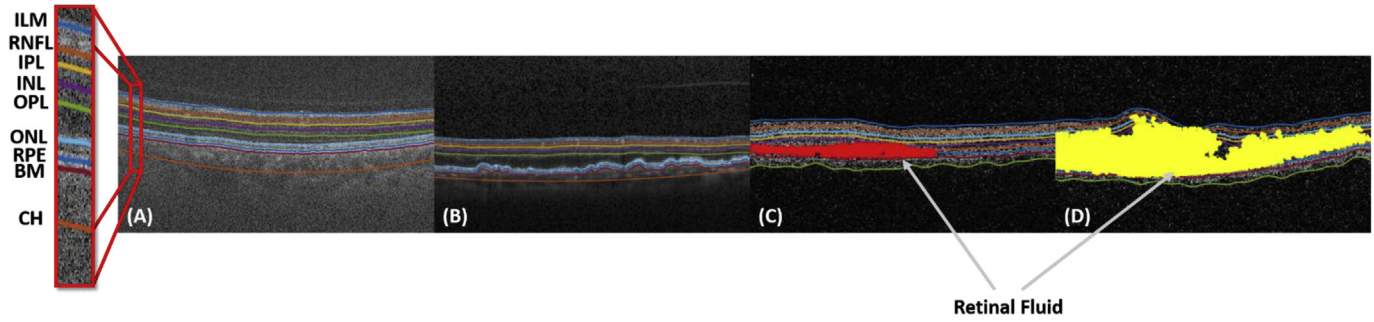

Fig. 1. Retinal OCT images: (A) normal OCT scan with labeled inner limiting membrane (ILM), retinal nerve fiber layer (RNFL), inner plexiform layer (IPL), inner nuclear layer (INL), outer plexiform layer (OPL), outer nuclear layer (ONL), retinal pigment epithelium (RPE), Bruch's membrane (BM), and choroid (CH); (B) AMD-affected OCT scan; (C) CSR-affected OCT scan (serous fluid is highlighted in red color); and (D) ME-affected OCT scan (cyst fluid is highlighted in yellow color).

the human retina [6]. Fig. 1 shows the OCT brightness scans (B-scans) of healthy and diseased subjects.

The rest of the paper is organized as follows. Section 2 presents the related work, and section 3 describes the detailed implementation of CNN-STGS. Evaluation results are presented in section 4, followed by a detailed discussion against the state-of-the-art solutions in section 5. Section 6 concludes the paper.

2. Related work

Many clinicians have studied OCT imaging and its usage for effectively diagnosing maculopathy. Wei Zhang et al. [7] discussed the usage of OCT in diagnosing DME. Shrestha et al. [8] reported a study on 35 patients in which they evaluated the OCT imagery for the diagnosis of clinically significant macular edema (CSME) and concluded that OCT is effective for evaluating CSME subjects. Nils F. Mokwa et al. [9] compared the grading of age-related macular degeneration (AMD) and choroidal neovascularization (CNV) with FA, FP, and spectral domain OCT (SD-OCT) imaging and concluded that FP is a valuable tool in identifying drusen and other pigmentary symptoms but that SD-OCT is also sensitive to CNV and AMD symptoms. Rosana Z. Hannouche et al. [10] compared different eye testing techniques to diagnose DME, and their concluding remarks were that OCT imaging is effective as compared with noncontact slit lamp biomicroscopy for diagnosing mild foveal edema. Desislava K. Georgieva [11] gave a detailed visualization of retinal pathology for the diagnosis of DME. Yasser M. Helmy et al. [12] considered the OCT scans of 104 eyes of age groups between 50 and 71 years and concluded that OCT imagery is effective for the visualization of cyst pathology. Gianni Virgili et al. [13] used OCT imaging for the detection of DME and CSME in patients suffering from diabetic retinopathy (DR). They considered 1325 eyes of 768 patients in their study and concluded that although the central retinal measurements through OCT imagery are inaccurate for diagnosing central CSME, the false positives show symptoms of DME, which cannot be diagnosed clinically [13]. Bartosz L. Sikorski et al. [14] studied OCT imaging for detecting diabetic maculopathy (DM) and concluded that OCT imaging can provide early detection of ME for the follow-up of DM. George Trichonas et al. [15] gave an overview of ME OCT profiles and presented the retinal layer features in vivo. They concluded that OCT is a new noninvasive technique for accurately evaluating ME. Michael R. Hee et al. [16] proposed a diagnosis system to screen DME patients using OCT images. They tested 182 eyes of 107 patients suffering from DR, 55 eyes from 31 patients with diabetes but without retinopathy, and 73 eyes of 41 normal subjects. Their concluding remark is that OCT is an effective technique to measure thickness variations in DME cases. Adam Martidis et al. [17] studied the use of intravitreal triamcinolone injection for treating DME. They considered 16 eyes with moderate CSME symptoms and concluded that intravitreal triamcinolone is a promising therapeutic method for treating DME patients.

Furthermore, many researchers have presented autonomous methods for the analysis of the human retina using OCT imagery. Li Zhang et al. [18] utilized adaptive boosting and graph cuts for diagnosing intraretinal CME and macular hole from 3-D OCT images. They achieved the true positive volume fraction, false positive volume fraction, and accuracy ratings of 84.6%, 1.7%, and 99.7%, respectively. Gray R. Wilkins et al. [19] manually extracted ILM and RPE layers for segmenting intraretinal fluid (IRF). The dataset used in their research consists of 16 subjects with the sensitivity ratings of 91% and specificity ratings of 96%. Jathurong Sugruk et al. [20] proposed a fully automated system to detect DME and AMD. To detect AMD, they extracted an RPE layer from macular OCT scans, while to diagnose DME, they extracted cysts from macular pathology. They reported an accuracy of 100% for the detection of AMD cases and 86.6% for those DME cases. Bilal Hassan et al. [21] diagnosed ME with the sensitivity and specificity of 100% and 86.67%, respectively. Delia. C. Fernández et al. [22] used structure tensors combined complex diffusion filtering to segment intraretinal pathology from healthy retinal OCT images. Their proposed system was effective in denoising the images and enhancing the retinal cellular structures. Stephanie J. Chiu et al. [23] used the graph theory and dynamic programming (GTDP) to segment up to eight layers from normal OCT images. Qi Yang et al. [24] presented a novel technique for segmenting retinal boundaries from OCT images of healthy subjects. They employed dual-scale gradient information for the segmentation of retinal layers. Appaji M. Abhishek et al. [25] presented a method to detect edema from SD-OCT images by measuring the thickness between ILM and RPE. Djibril Kaba et al. [26] presented a method to evaluate the retinal thickness profile within the optic disc region. Their method achieved an average Dice coefficient of 0.9468 pixels for extracting RNFL thickness. Yijun Huang et al. [27] presented a method to detect DME from OCT scans by extracting the retinal layers. They applied their proposed system on SD-OCT images of 28 eyes, where 24 patients were suffering from DME and 4 were healthy subjects. They validated their method using the Wilcoxon test [27]. Pratul P. Srinivasan et al. [28] diagnosed AMD and DME pathologies using supervised support vector machine (SVM) classifier. They have correctly classified 100% DME cases; however, for healthy cases, their accuracy remained 86.67%. Stephanie J. Chiu et al. [29] presented a kernel regression and graph theory dynamic programming (KR + GTDP) framework for segmenting retinal layers and retinal fluids. KR + GTDP was tested on publicly available Duke Dataset-II that contains 610 OCT B-scans of 10 patients having severe DME. Leyuan Fang et al. [30] proposed a framework based on convolutional neural network (CNN) and graph search methods (CNN-GS) for extracting retinal layers from AMD subjects. Abdolreza Rashno et al. [31] presented an automated extraction of cyst/fluid from DME-affected OCT images. Cecilia S. Lee et al. [32] proposed a method for segmenting retinal fluid from OCT images. They applied their method to 1289 retinal scans. Thomas Schlegl et al. [33] developed a semantic segmentation-based method to analyze intraretinal and subretinal fluid segments from 1200 OCT volumes of

AMD, DME, and retinal vein occlusion (RVO) patients, and the scans were acquired from Zeiss Cirrus and Heidelberg Spectralis OCT machines [33]. Abhijit G. Roy et al. [34] presented a fully convolutional network (ReLayNet) for extracting retinal information from macular OCT images.

We have also developed fully automated algorithms to detect and diagnose various macular diseases based on a multilayered support vector machine (SVM) classification model [35–37]. Here, we present a deep CNN and structure tensor graph search-based segmentation framework (CNN-STGS) for extracting and evaluating nine retinal layers, cyst and serous pathology, followed by the automated 3-D profiling. Although the system proposed in Ref. [29] can automatically extract up to seven intraretinal layers and retinal fluid, the mean Dice coefficient achieved by their model for fluid extraction is not tempting, also highlighted in Ref. [32]. The system proposed in Ref. [30] was only applied to AMD-affected scans for segmenting retinal layers. The neutrosophic sets and graph algorithms-based framework proposed in Ref. [31] was also compared with [29], where it produced better results in terms of Dice coefficient and precision. The model proposed in Ref. [32] was utilized for the extraction of cyst fluid from OCT B-scans; however, the computational time complexity of their proposed system is unpersuasive. Furthermore, they have only used deep learning-based visual analysis for the extraction of cyst fluid. The model proposed in Ref. [33] not only detect macular fluids, but it also quantifies them as intraretinal or subretinal with the mean accuracy of 0.94 and 0.92, respectively. However, it does not extract retinal layers, and the authors have only tested the fluid extraction and quantification on three types of macular pathologies. The extraction of retinal layers significantly assists in the localization of macular fluids, and it provides a complete 3-D presentation of the human retina, which ultimately leads to more accurate, in-depth, and objective diagnosis of retinal pathology. ReLayNet [34], on the other hand, can segment retinal layers and retinal fluids; however, it was validated only on Duke Dataset-II [29] containing scans of DME subjects. CNN-STGS not only outperformed all the existing work significantly, but it is also a framework that provides a robust characterization of retinal fluids as well as the complete 3-D profiling of the normal and diseased human retina. Table 1 shows the detailed summary of automated methods, which have been proposed in the past, along with their limitations that have been addressed by the proposed CNN-STGS framework.

CNN-STGS fulfills all the research gaps that have been highlighted in Table 1. Apart from this, the main contributions of this paper are shown below:

- This paper proposes a CNN-STGS framework that can segment nine retinal layers from SD-OCT images depicting different types of retinal pathologies.
- The model proposed in Ref. [34] can segment seven retinal layers and fluid segments from Duke Dataset-II [29]. The proposed CNN-STGS not only extracts seven retinal layers and retinal fluids from Duke Dataset-II, but it is also the framework that is tested on four publicly available datasets having different types of retinal pathologies. To the best of our knowledge, CNN-STGS is the first of its kind that extracts retinal information from healthy and AMD-, ME-, and CSR-affected scans acquired through different OCT machines.
- Furthermore, CNN-STGS not only extracts retinal fluids, but it also characterizes them as serous and cyst, which ultimately leads to the automated diagnosis of CSR and ME pathologies.
- Apart from this, CNN-STGS is the only framework that provides a complete suite for the extraction and characterization of retinal layers and fluid pathology, followed by a 3-D presentation of the human retina.
- CNN-STGS is applied to 46,541 B-scans, and it is among the fastest and robust 3-D integrated solution capable of picking small retinal fluid variations and low-intensity layer information.
- CNN-STGS significantly outperforms the state-of-the-art solutions with up to 11.70% improvements on publicly available Duke datasets for the extraction of retinal fluid pathology.

3. Proposed implementation

A deep structure tensor graph search-based segmentation framework (CNN-STGS) is proposed here for extracting and characterizing retinal anomalies from OCT B-scans. Fig. 2 shows the block diagram that includes all the modules of the proposed framework. First of all, CNN-STGS extracts retinal layers from OCT volume. Afterward, the extracted layers are used for 3-D profiling as well as for the extraction of retinal fluids. Since maculopathy-based fluid segments are mostly present within the neurosensory retina, therefore, CNN-STGS uses the segmented retinal nerve fiber layer (RNFL) and retinal pigment epithelium (RPE) to extract the neurosensory retina. The fluid segments from the isolated neurosensory retina are extracted from the probability maps and are further classified as a cyst or serous using a deep CNN model. Furthermore, CNN-STGS utilizes segmented retinal layers for reconstructing a 3-D representation of the human retina. CNN-STGS was validated on different publicly available datasets containing SD-OCT scans, which are acquired through OCT machines of different vendors.

3.1. Material

CNN-STGS has been validated on four different datasets that are publicly available online. Duke datasets were acquired using Spectralis, Heidelberg Inc., while the Armed Forces Institute of Ophthalmology (AFIO) dataset was acquired using Topcon 3-D OCT 2000 series. Duke datasets contain normal as well as DME- and AMD-affected scans, while AFIO dataset contains scans with healthy, ME, and CSR pathology. Apart from this, all these datasets are thoroughly marked by multiple expert ophthalmologists. Detailed information about the datasets is presented in Table 2.

3.2. Structure tensor graph search (STGS) framework

The prime objective of developing the STGS framework is to accurately segment retinal layers from OCT B-scans irrespective of their acquisition machinery, their quality, or the pathology that they depict. To demonstrate STGS, let us consider an image $I \in \mathbb{R}^{MxN}$ (M and N denote the height and width of I, respectively) that has been denoised using an adaptive 2-D Wiener filter, which estimates the local mean and variance within the neighborhood of each original pixel $\rho(u_i, v_i)$ as expressed in Eqs. (1)–(3):

$$\mu = \frac{1}{\omega_u \omega_v} \sum_{u_i \in \omega_u} \sum_{v_j \in \omega_v} \rho(u_i, v_i) \tag{1}$$

$$\sigma^2 = \frac{1}{\omega_u \omega_v} \sum_{u_i \in \omega_u} \sum_{v_j \in \omega_v} \rho^2(u_i, v_i) - \mu^2 \tag{2}$$

$$\gamma(u_i, v_i) = \mu + \frac{\sigma^2 - v^2}{\sigma^2}(\rho(u_i, v_i) - \mu) \tag{3}$$

where $\gamma(u_i, v_i)$ is the denoised pixel within I, ω_u and ω_v respectively represent the vertical and horizontal axis of denoising window, μ represents the local estimated mean, σ^2 represents the local estimated variance, and v^2 is the average of σ^2 [36]. The size of the denoising window is empirically chosen to be 51×211, and it remains the same for all the datasets. After denoising, to highlight layers, STGS first computes four nonoverlapping orthogonal tensors as expressed in Eqs. (4)–(7) [39]:

$$\delta = \begin{bmatrix} T_{XX}^2 & T_{XY} \\ T_{YX} & T_{YY}^2 \end{bmatrix} \tag{4}$$

Table 1
Detailed summary of existing work.

Methods	Contributions	Gaps
[18]	They used adaptive boosting and graph cuts for diagnosing intraretinal CME and macular hole from 3-D OCT images.	They have not extracted retinal layers and retinal fluids from the OCT scans of different datasets.
[19]	They detected IRF by manually segmenting ILM and RPE.	They have not extracted retinal layers from the OCT scans of different datasets.
[20]	They proposed a fully automated system to detect DME and AMD. To detect AMD, they extracted an RPE layer from macular OCT scans, while to diagnose DME, they extracted cysts from macular pathology.	They have not extracted retinal layers and retinal fluids from the OCT scans of different datasets.
[21]	They used gradients and linear discriminant analysis for the classification of ME.	They have not extracted retinal layers and retinal fluids from the OCT scans of different datasets.
[22]	They used structure tensors combined complex diffusion filtering to segment intraretinal pathology from healthy retinal OCT images.	They have not extracted the retinal layers and retinal fluids from the OCT scans of diseased subjects.
[23]	They used the graph theory and dynamic programming (GTDP) to segment up to eight retinal layers from spectral domain healthy OCT images.	They have not extracted the retinal layers and retinal fluids from the OCT B-scans of diseased subjects.
[24]	They presented a novel method to extract retinal boundaries from the OCT scans of a normal person. They employed dual-scale gradient information for the segmentation of retinal layers.	They have not extracted the retinal layers and retinal fluids from the OCT B-scans of diseased subjects.
[25]	They presented an automated method to detect edema from SD-OCT images by measuring the thickness between ILM and RPE.	They have not extracted retinal layers and retinal fluids from the OCT scans of different datasets.
[26]	They presented an automated method based on kernel graph cuts to evaluate retinal thickness profile within the optic disc region.	They have not extracted retinal layers and retinal fluids from the OCT scans of different datasets.
[27]	They presented a semi-automated method to segment retinal layers from SD-OCT images to detect DME.	They have not extracted retinal layers and retinal fluids from the OCT scans of different datasets.
[28]	They utilized the SVM classification model for the diagnosis of AMD and DME pathologies from OCT images.	They have not extracted retinal layers and retinal fluids from the OCT scans of different datasets.
[29]	They presented a KR + GTDP framework for segmenting retinal layers and retinal fluids from the OCT scans of 10 subjects having severe DME.	They have not extracted retinal layers and retinal fluids from maculopathy-affected scans other than those depicting DME pathology.
[30]	They proposed a CNN-GS framework for extracting retinal layers from AMD-affected OCT scans.	They have not extracted retinal layers from maculopathy-affected scans other than those depicting nonexudative AMD pathology.
[31]	They proposed an automated extraction cyst/fluid from DME-affected OCT images using neutrosophic sets and graph algorithms.	They have not extracted retinal layers and retinal fluids from maculopathy-affected scans other than those depicting DME pathology.
[32]	They proposed a deep learning-based visual analysis and segmentation of cyst fluid from 1289 OCT images.	They have not extracted retinal layers from OCT scans irrespective of their acquisition machinery or their quality. Also, they have not extracted and identified fluid information from diseased scans other than those depicting DME pathology.
[33]	They developed a semantic segmentation-based fully automated method to detect and quantify intraretinal fluid and subretinal fluid from 1200 OCT volumes of AMD, DME, and RVO patients.	They have not extracted retinal layers from healthy or diseased OCT scans of different datasets.
[34]	They presented fully convolutional network (ReLayNet) for extracting retinal information from macular OCT images.	ReLayNet was only applied on Duke Dataset-II [29] for the extraction of retinal layers and fluid information from OCT scans of DME subjects.
[35–37]	We proposed automated methods to predict healthy and diseased scans, along with extracting retinal information.	No generalized framework presented that could extract nine layers, along with the extraction and identification of intraretinal and subretinal fluids from scans acquired through different OCT machinery.

$$T^2_{XX} = \sum_{x_i \in \varphi_x} \sum_{y_j \in \varphi_j} w(x_i,\ y_j)\ T_{\varphi X} \tag{5}$$

$$T_{XY} = T_{YX} = \sum_{x_i \in \varphi_x} \sum_{y_j \in \varphi_j} w(x_{i,} y_j)\ T_{\varphi XY} \tag{6}$$

$$T^2_{YY} = \sum_{x_i \in \varphi_x} \sum_{y_j \in \varphi_j} w(x_i, y_j)\ T_{\varphi Y} \tag{7}$$

where δ is the second-order tensor grid, T^2_{XX} represents the square of horizontal image gradients, T_{XY} and T_{YX} respectively represent the product of horizontal and vertical gradients, T^2_{YY} represents the square of vertical image gradients [39], and $w(x, y)$ denotes a localized Gaussian window for the defined neighborhood of 11×11 (chosen empirically). $T_{\varphi Y}$, $T_{\varphi XY}$, and $T_{\varphi X}$ represent the directional derivatives of the denoised scan within the specified neighborhood, also represented mathematically through Eqs. (8)–(10):

$$T_{\varphi Y} = \left(I^{'}_{Y}(x - x_i, y - y_j)\right)^2 \tag{8}$$

$$T_{\varphi XY} = \left(I^{'}_{X}(x - x_i, y - y_j)\right)\left(I^{'}_{DY}(x - x_i, y - y_j)\right) \tag{9}$$

$$T_{\varphi X} = \left(I^{'}_{X}(x - x_i, y - y_j)\right)^2 \tag{10}$$

where $I^{'}_{X}$ and $I^{'}_{Y}$ are the horizontal and vertical gradients of I. Each tensor in δ depicts the respective predominant orientation of the underlying image object (layers), and the maximum coherency will be in that tensor that captures the maximum amount of object information [40].

In majority cases, all the layers within the scan are oriented horizontally. Therefore, tensor T_{YY} will have the maximum retinal information. However, the STGS framework does not rely on this information; instead, it automatically computes the degree of coherency from each tensor through the set of extracted eigenvalues [40] and pick that tensor that has the highest coherency [40]. Fig. 3 shows the B-scans that are denoised and are processed by the STGS framework. From Fig. 3, it can be observed that denoising the scan through an adaptive Wiener filter removes the speckle noise due to which only the layers information is highlighted, and the layers are separated from one another within the selected tensor. Afterward, STGS binarizes the selected tensor and converts it into an undirected graph with each node representing the pixel that is connected to another node (pixel) through an edge. The edge information within a graph is maintained through the respective adjacency matrix. STGS then automatically initializes the image's top and bottom rows as seed points that proceed toward convergence by picking retinal layer pixels iteratively. In each iteration, the seed points are updated by computing the absolute difference between the current node value and its neighbors. If the difference between the top row seed points and all their neighbors is the same, then the top seed points are updated to a node that corresponds to the downward pixel in T_{YY} . Likewise, the bottom row seed points are updated to the nodes representing an above pixel, if all their neighbors have the same values. When the seed points observe a change in the foreground and background pixel (when the edge weights are not the

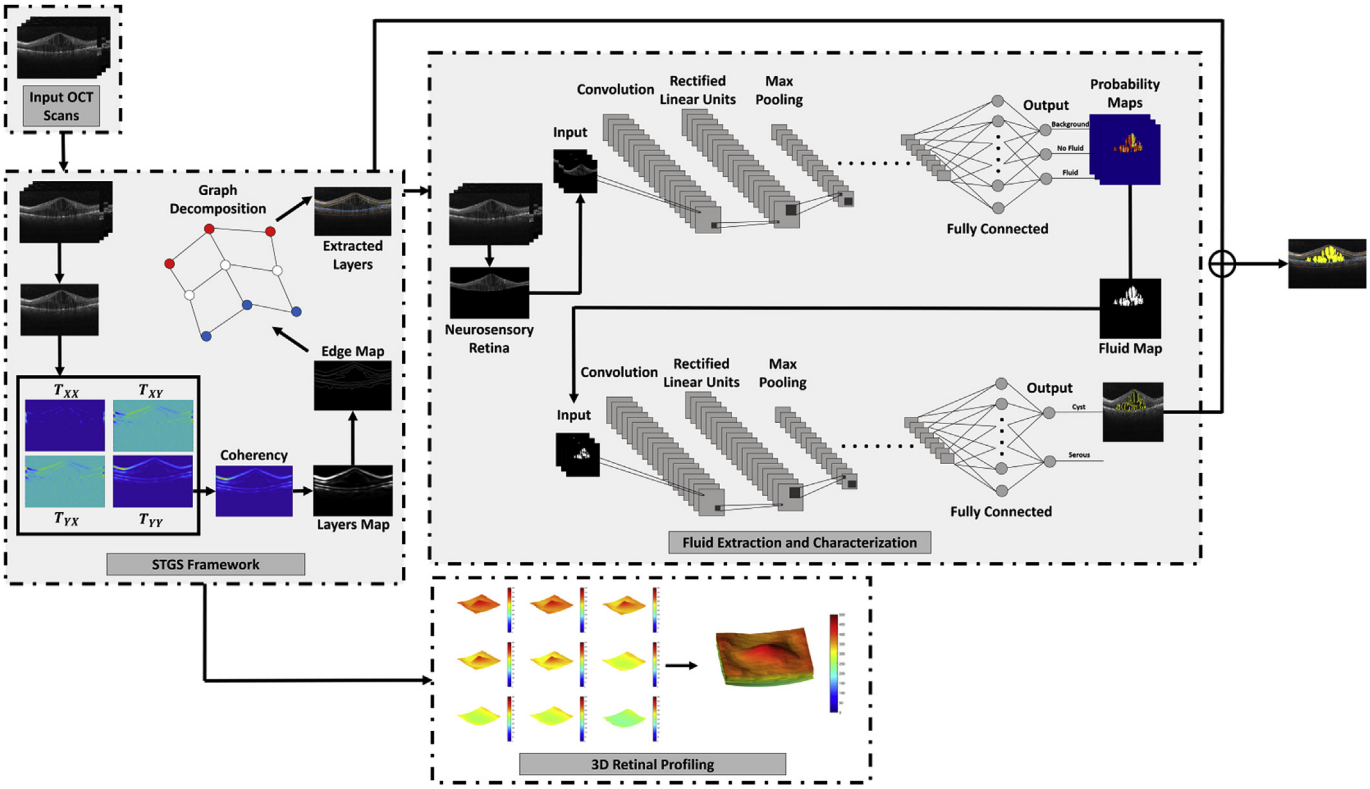

Fig. 2. Block diagram of CNN-STGS for the analysis and 3-D presentation of the human retina.

same), then STGS considers the respective pixel as part of the layer. The whole graph search algorithm converges when the initialized seed points overlap one another as shown in Fig. 4, where $\tau_{i,j}$ represents the iterations of the graph search algorithm in which i denotes the passes and j denotes the iterations in each pass. STGS can segment retinal layers even from the highly degraded scans as well.

At any point z, if STGS misses the layer σ_z, it is automatically estimated through the fitted polynomial expressed in Eqs. (11)–(16):

$$\sigma_z = \sum_{i=0}^{n} \beta_i z^i = \beta_0 + \beta_1 z + \ldots + \beta_n z^n \tag{11}$$

$$\beta = [\beta_0, \beta_1, \beta_2, \ldots, \beta_n]^T \tag{12}$$

where β is the unknown coefficient that is extracted through

$$J\beta = \sigma \tag{13}$$

$$\sigma = [\sigma_0, \sigma_1, \sigma_2, \ldots, \sigma_n]^T \tag{14}$$

$$\beta = J^{-1}\sigma \tag{15}$$

and

$$J = \begin{bmatrix} 1 & z_0 & z_0^2 & z_0^3 & z_0^4 & \cdots & z_0^n \\ 1 & z_1 & z_1^2 & z_1^3 & z_1^4 & \cdots & z_1^n \\ 1 & z_2 & z_2^2 & z_2^3 & z_2^4 & \cdots & z_2^n \\ \vdots & \vdots & \vdots & \vdots & \vdots & \cdots & \vdots \\ \vdots & \vdots & \vdots & \vdots & \vdots & \cdots & \vdots \\ 1 & z_{n-1} & z_{n-1}^2 & z_{n-1}^3 & z_{n-1}^4 & \ddots & \vdots \\ 1 & z_n & z_n^2 & z_n^3 & z_n^4 & \cdots & z_n^n \end{bmatrix} \tag{16}$$

J depicts the n^{th} order polynomial generated through $n+1$ layer points, and σ denotes the $n+1$ layer points near z. Apart from this, Fig. 8 shows the retinal layers that are extracted through the proposed STGS algorithm for different retinal pathologies.

3.3. Fluid extraction and characterization

The second phase of CNN-STGS is the extraction of retinal fluid from retinal OCT scans. To extract the fluid pathology, CNN-STGS automatically generates a mask $B \in \mathbb{R}^{MxN}$ using the extracted RNFL and RPE layers. The response of B is designed in such a way that when it is multiplied with an OCT scan, their product yields an image B_M that only

Table 2
Dataset description.

Name	Pathologies	Scans	B-Scans Dimension (pixel × pixel)	Subjects	Acquisition Machine	URL
Duke Dataset-I	AMD	26,900	1000 × 512	269	Spectralis	http://people.duke.edu/~sf59/RPEDC_Ophth_2013_dataset.htm [38]
	Normal	11,500		115		
Duke Dataset-II	DME	610	768 × 496	10	Spectralis	http://people.duke.edu/~sf59/Chiu_BOE_2014_dataset.htm [29]
Duke Dataset-III	AMD	763	512 × 496	15	Spectralis	http://people.duke.edu/~sf59/Srinivasan_BOE_2014_dataset.htm [28]
	DME	1101		15		
	Normal	1407		15		
AFIO Dataset	ME	2195	951 × 456	11	Topcon 3-D OCT 2000 Series	http://biomisa.org/index.php/biomisa-retinal-image-database-for-retinopathy/ [43]
	CSR	1161		9		
	Normal	904		31		

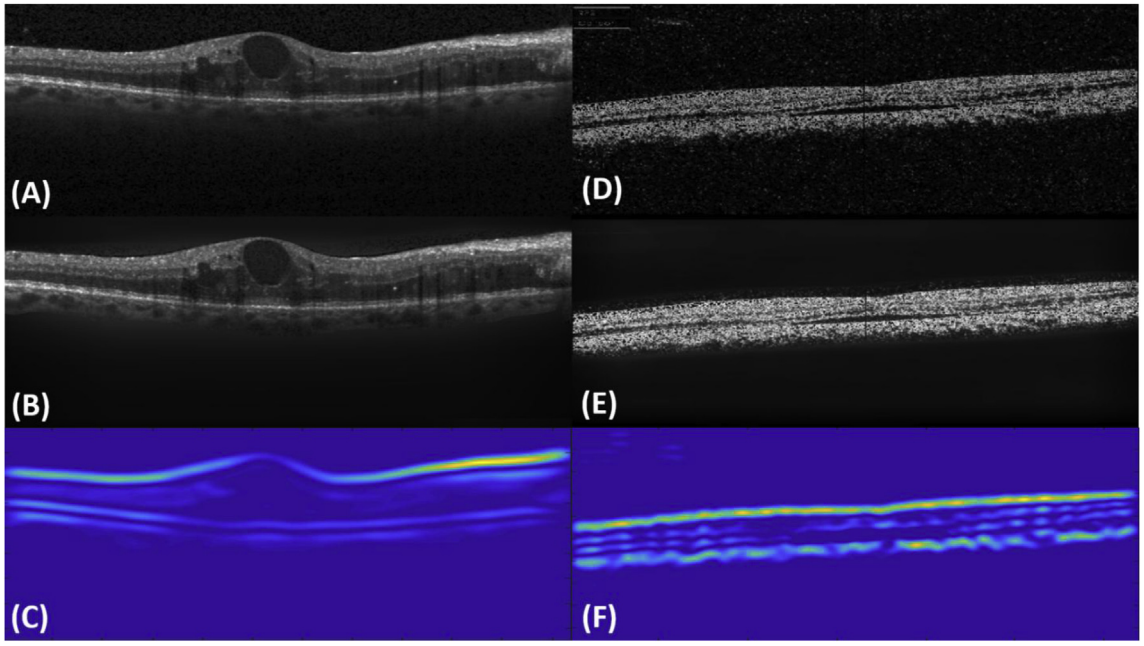

Fig. 3. (A) Original scan from Duke Dataset-II, (B) scan denoised through an adaptive Wiener filter, (C) layers information within the selected tensor, (D) original scan from AFIO Dataset, (E) scan denoised through an adaptive Wiener filter, (F) layers information within the selected tensor.

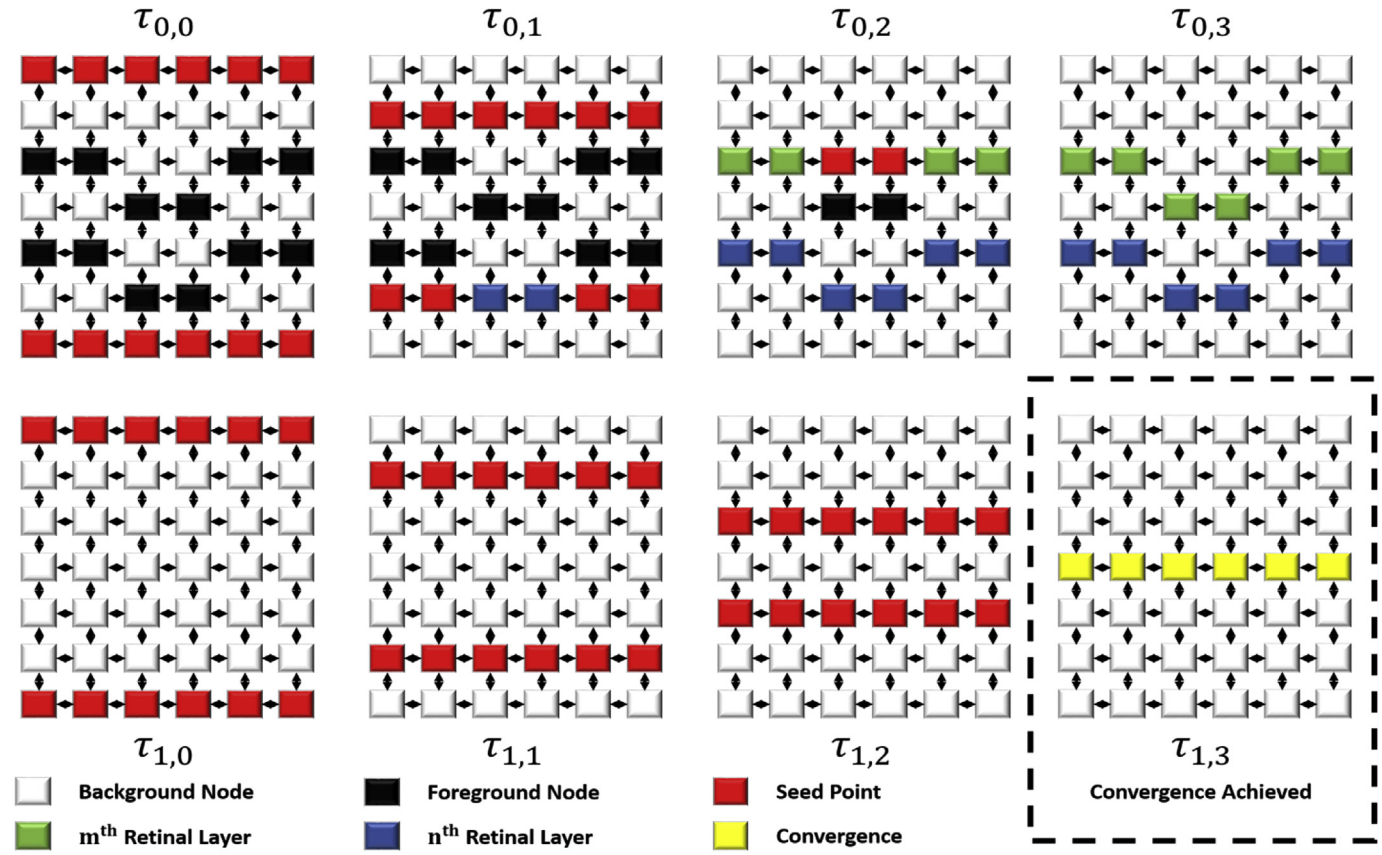

Fig. 4. Structure tensor graph search (STGS) traversal. In each iteration, the seed points are updated by computing the absolute difference between the current node value and its neighbors. If the difference between the top row seed points and all their neighbors is the same, then the top seed points are updated to a node that corresponds to the downward pixel in T_{YY} through respective adjacency matrix. Likewise, the bottom row seed points are updated to the nodes representing an above pixel, if all their neighbors have the same values. When the seed points observe a change in foreground and background pixel, then STGS considers the respective pixel as part of the layer.

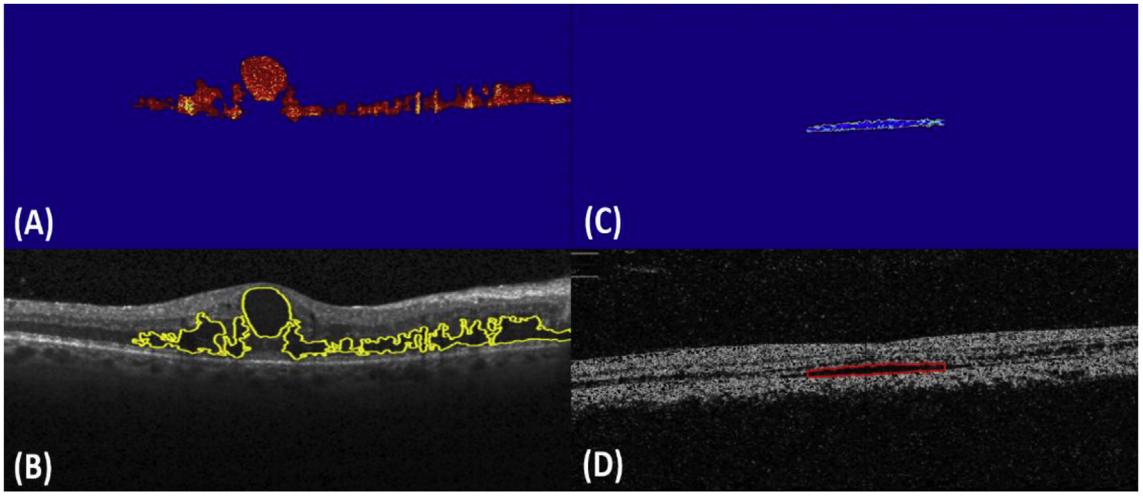

Fig. 5. Retinal fluid extraction and identification: (A) probability map of cyst fluid, (B) cyst fluid mapped on the original B-scan, (C) probability map of serous fluid, and (D) serous fluid mapped on the original B-scan.

contains the isolated neurosensory retina as expressed in Eqs. (17) and (18):

$$B_M = B\ x\ I \tag{17}$$

$$\begin{bmatrix} B_{M1,1} & \cdots & B_{M1,n} \\ \vdots & \ddots & \vdots \\ B_{Mn,1} & \cdots & B_{Mn,n} \end{bmatrix} = \begin{bmatrix} B_{1,1} & \cdots & B_{1,n} \\ \vdots & \ddots & \vdots \\ B_{n,1} & \cdots & B_{n,n} \end{bmatrix} \mathrm{x} \begin{bmatrix} I_{1,1} & \cdots & I_{1,n} \\ \vdots & \ddots & \vdots \\ I_{n,1} & \cdots & I_{n,n} \end{bmatrix} \tag{18}$$

B_M is then passed to the trained regional convolutional neural network (RCNN) model that segments B_M into the fluid region, the no-fluid region, and the background region with the associated probabilities. If the neurosensory image B_M contains any fluid segments, then the respective fluid probability map is binarized, and it is characterized as a cyst or serous fluid using the second layer of the CNN model. CNN-STGS utilizes a pre-trained AlexNet CNN model [41] for the extraction and characterization of fluid that has been trained on the custom training dataset through transfer learning. The detailed architectural description of AlexNet is presented in Ref. [41], whereas the auto-generated fluid probability maps for two of the randomly selected B-scans are shown in Fig. 5, which are further characterized as a cyst and serous, respectively. One of the key benefits of CNN-STGS is that it is extremely robust in detecting small retinal fluid variations, and it not only detects them, but it is also able to characterize them as a cyst or serous, which automatically leads to the grading of OCT volume as ME- or CSR-affected. Table 3 shows the hyperparameters of the CNN models that have been fine-tuned after the rigorous experiments. Apart from this, the optimization function utilized in the proposed framework is the stochastic gradient descent (SGD) [42].

3.4. 3-D presentation of the human retina

The STGS framework can accurately extract nine layers from OCT B-scans of which two layers are used to extract fluid pathology. Furthermore, CNN-STGS utilizes the extracted retinal layers for the reconstruction of 3-D retinal surfaces as shown in Fig. 6. Whenever the OCT volumetric scan is loaded, CNN-STGS processes it frame by frame, and from each frame, it extracts nine retinal layers. These layers are stored into the respective layer image $S_q \in \mathbb{R}^{MxN}$, where M denotes the B-scans, N denotes axial scans (A-scans), and q denotes the retinal layer index, whose value ranges from $1 \leq q \leq 9$. After constructing the layer images, the 3-D profiles are generated $RS_q \in \mathbb{R}^{MxNxK}$, where the third axis K is automatically generated from S_q intensities. Afterward, these surfaces are inverted and merged together for the 3-D presentation of the human retina. Furthermore, the extracted ILM and RPE are also used to generate the overall retinal thickness surface to present an objective visualization of macular pathology as shown in Fig. 6.

4. Results

CNN-STGS is validated on multiple publicly available datasets as explained in section 3.1. The evaluations on all these datasets were performed at multiple levels, that is, first, for the segmentation of retinal layers and then for the extraction and characterization of fluid pathology. Table 4 contains the mean accuracy α_k for segmenting k^{th} retinal layer for each syndrome from AFIO dataset. The mean accuracy α_k for a k^{th} layer is computed by averaging the relative error as expressed below:

$$\alpha_k = 1 - \frac{\left(\sum_{i=0}^{A_s-1} \frac{|\eta_{i,k} - \eta'_{i,k}|}{|\eta_{i,k}|}\right)}{A_s} \tag{19}$$

where $\eta_{i,k}$ denotes the value of i^{th} axial scan (A-scan) and k^{th} layer annotation, $\eta'_{i,k}$ shows the value of i^{th} A-scan and k^{th} layer extracted through CNN-STGS, and A_s denotes the number of A-scans. From Table 4, it can be seen that CNN-STGS extracts the retinal layers with up to 94% mean accuracy.

Apart from this, Table 5 shows the comparison of CNN-STGS for the extraction of retinal layers with the state-of-the-art solutions. All the methods in Table 5 have been validated on publicly available Duke Dataset-II. The values in Table 5 are shown in both pixels and micrometers ($\mu\ m$), and they are computed by taking the absolute difference between the extracted layers and the marked annotations.

From Table 5, it can be observed that CNN-STGS obtained the best segmentation results for RNFL, GCL-IPL, OPL, ONL-ISM, and OS-RPE.

Table 3
Hyperparameters tuned for cnn-stgs.

Model	Learning Rate	Convolution	ReLU	Dropout	Convolution Kernels	Max Pooling	Fully Connected	Optimizer	Loss Function
RCNN CNN	1^{-6} 10^{-4}	5	7	2	11 × 11, 5 × 5, 3 × 3	3	3	SGD	Cross entropy

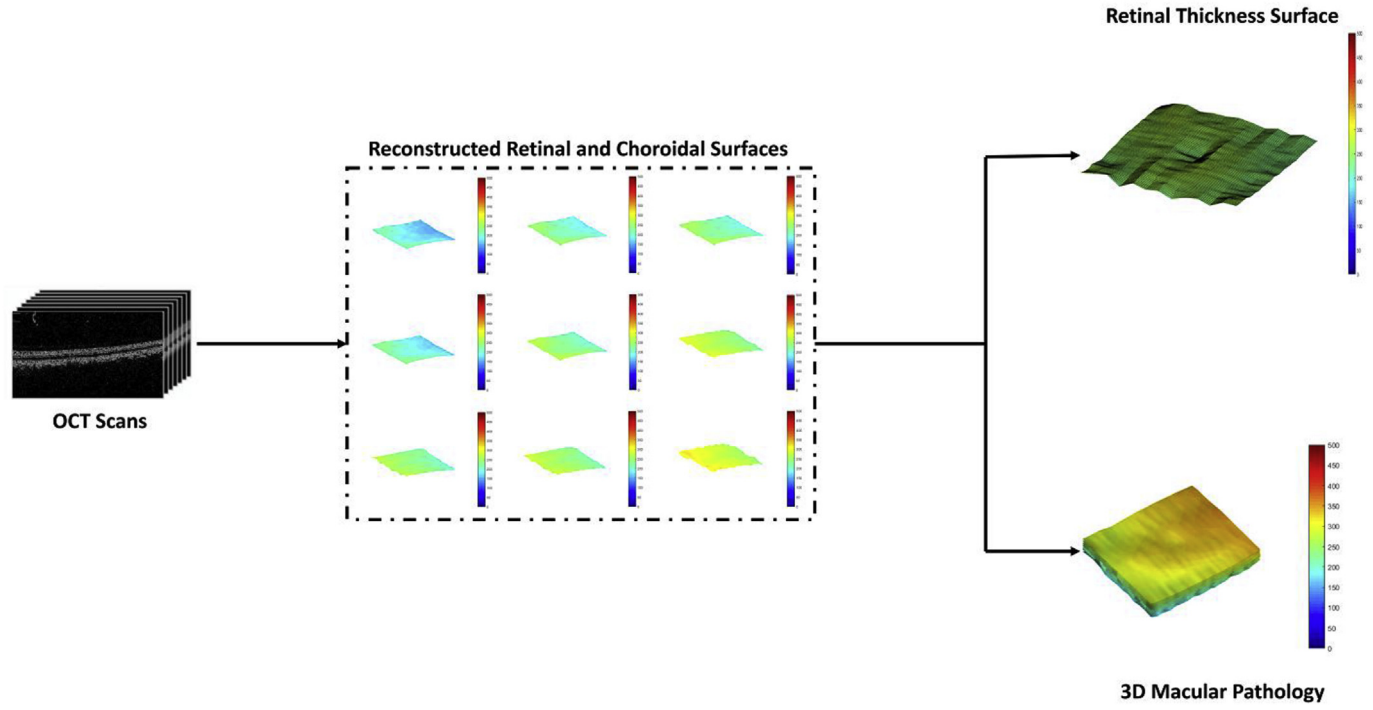

Fig. 6. Automated 3-D presentation of the CSR-affected human retina.

The second-best results are produced by the framework proposed in Ref. [34]; however, it should be noted here that the results produced by Ref. [34] in Table 5 are only against clinician 1 annotations, whereas the results of CNN-STGS are obtained by taking the mean of the segmentation results from both clinicians as evident in Table 5. Apart from this, Table 6 shows the performance of CNN-STGS for the extraction of fluid pathology on Duke Dataset-II [29] through the mean Dice coefficient. The inter-manual mean Dice coefficient of both clinicians on Duke Dataset-II was 0.58 ± 0.32 [29], which indicates significant variability in the fluid annotations itself. Thus, to overcome this, we acquired another set of fluid annotations on Duke Dataset-II from the third expert ophthalmologist and kept those two sets, which highly correlate with each other as shown in Table 6. However, for comparing CNN-STGS fluid extraction against state-of-the-art solutions, we utilized the original annotations, where CNN-STGS achieved the overall mean Dice coefficient of 0.647 ± 0.105, which is 11.70% better than [29] and 3.7% better than [31].

From Table 6, it can be observed that CNN-STGS was able to achieve an overall mean Dice coefficient of 0.7813 ± 0.0508, whereas the Dice coefficient achieved by Ref. [32] was 0.729, and the Dice coefficient achieved by Ref. [34] was 0.77. However, the comparison with [32] is indirect as the result obtained in Ref. [32] is on the dataset that is not publicly available; nonetheless, the Dice coefficient achieved by Ref. [34] was on Duke Dataset-II [29] against clinician 1 markings. It can be clearly observed from Table 6 that CNN-STGS achieved 1.59% better results as compared with [34], which is significant, especially considering the fact that CNN-STGS is able to extract nine layers, along with fluid pathology, from multi-vendor OCT scans depicting different retinal pathologies, whereas [34] achieved its results only on Duke Dataset-II acquired from the Spectralis machine by Heidelberg Inc. Therefore, one of the key features of CNN-STGS is that it can work on SD-OCT scans irrespective of OCT machines. We have tested and validated CNN-STGS on AFIO dataset that is acquired through Topcon 3-D OCT 2000 series. It should be noted here that the scans within AFIO dataset were of poor quality as compared with Duke Dataset-I, II, and II; however, CNN-STGS was easily able to extract retinal information from AFIO dataset containing different retinal pathological conditions. To the best of our knowledge, most of the work has been done for the extraction of cyst fluid from DME-affected scans. However, in the majority cases, the cyst fluid is not the only fluid present within the retina. CNN-STGS is unique that it can differentiate between the cyst and serous fluid, which also leads to the automated grading between ME and CSR subjects. Since only AFIO dataset contains the scans from ME and CSR patients, along with their markings, therefore, in this paper, the performance of CNN-STGS for fluid characterization was only tested on AFIO dataset. Table 7 shows the mean Dice coefficient of CNN-STGS, and the Dice coefficients were computed against the manual markings done by an expert ophthalmologist from AFIO, Rawalpindi, Pakistan.

Table 4
Accuracy for extracting retinal layers from oct scans having different pathological conditions.

Syndrome	Cases	ILM	RNFL/GCL	IPL	INL	OPL/ONL	IS/OS	RPE	BM	CHOROID
ME	Mean[a]	0.95	0.93	0.92	0.96	0.94	0.97	0.92	0.94	0.97
	STD[a]	0.04	0.03	0.01	0.03	0.04	0.02	0.01	0.05	0.01
CSR	Mean[a]	0.96	0.93	0.94	0.93	0.91	0.96	0.95	0.97	0.94
	STD[a]	0.03	0.04	0.03	0.03	0.01	0.03	0.04	0.02	0.01
Normal	Mean[a]	0.93	0.94	0.94	0.91	0.93	0.92	0.93	0.95	0.94
	STD[a]	0.02	0.03	0.05	0.04	0.05	0.03	0.04	0.02	0.03

[a] Values are computed for all the scans within the AFIO dataset.

Table 5
Comparison of layer segmentation on duke dataset-ii.

Unit	Layers	CNN-STGS against Clinician 1	CNN-STGS against Clinician 2	CNN-STGS Overall	Normal GTDP[a] [29]	KR + GTDP [29]	ReLayNet[b] [34]
Pixel	RNFL	1.05	0.81	0.93	7.44	1.06	1.50
	GCL-IPL	0.97	1.38	1.17	3.42	1.39	1.20
	INL	2.12	1.48	1.80	2.85	2.27	1.00
	OPL	1.01	1.59	1.30	1.87	1.82	1.31
	ONL-ISM	0.96	1.67	1.31	5.64	1.95	1.35
	ISE	0.61	0.63	0.62	0.72	0.82	0.62
	OS-RPE	0.72	0.99	0.85	1.01	1.04	0.92
μm	RNFL	3.64	2.81	3.22	25.8	3.68	5.20
	GCL-IPL	3.36	4.78	4.07	11.9	4.84	4.16
	INL	7.35	5.13	6.24	9.91	7.90	3.47
	OPL	3.50	5.51	4.52	6.50	6.35	4.54
	ONL-ISM	3.33	5.79	4.56	19.5	6.80	4.68
	ISE	2.11	2.18	2.14	2.53	2.88	2.15
	OS-RPE	2.49	3.43	2.96	3.51	3.61	3.19

[a] The original GTDP algorithm was published in Ref. [23]; however, in Ref. [29], the authors have improved their GTDP algorithm, and the presented results are shown for their improved implementation [29].
[b] The values of ReLayNet are computed only against clinician 1 [34].

Table 6
Mean dice coefficient of cnn-stgs on duke dataset-ii.

Subjects	Against Clinician 1 Mean (STD)	Against Clinician 2 Mean (STD)
1	0.8243 (0.0111)	0.7841 (0.0326)
2	0.7254 (0.0317)	0.7593 (0.0958)
3	0.7920 (0.0341)	0.7648 (0.0673)
4	0.7794 (0.0217)	0.7742 (0.0973)
5	0.7869 (0.0647)	0.7692 (0.0835)
6	0.7538 (0.0154)	0.7915 (0.0638)
7	0.7824 (0.0269)	0.7893 (0.0759)
8	0.8591 (0.0425)	0.8142 (0.0623)
9[a]	–	–
10	0.7697 (0.0438)	0.7427 (0.0451)
Overall	**0.7859 (0.0324)**	**0.7766 (0.0693)**

[a] The Dice coefficient was not computed because no markings were available.

Table 7
Mean dice coefficient of cnn-stgs on afio dataset [43].

Subjects	Cyst Mean (STD)	Serous Mean (STD)
1	0.91 (0.0351)	0.87 (0.0478)
2	0.85 (0.0417)	0.93 (0.0586)
3	0.92 (0.0215)	0.92 (0.0354)
4	0.81 (0.0485)	0.96 (0.0824)
5	0.84 (0.0213)	0.95 (0.0943)
6	0.95 (0.0745)	0.91 (0.0247)
7	0.96 (0.0825)	0.93 (0.0784)
8	0.85 (0.0658)	0.94 (0.0149)
9	0.84 (0.0325)	0.93 (0.0965)
10	0.95 (0.0547)	0.90 (0.0678)
Overall	**0.888 (0.0478)**	**0.924 (0.0600)**

Table 8
Performance of fluid characterization on afio dataset [30].

Fluid	Scans	Accuracy	Sensitivity	Specificity
Cyst	704	98.75%	99.14%	98.61%
Serous	576			

It can be observed from Table 7 that CNN-STGS is quite robust in extracting fluid segments with the mean Dice coefficient of 0.906 ± 0.0539. Furthermore, CNN-STGS is able to distinguish between cyst and serous with the accuracy of 98.75% as shown in Table 8.

Table 9
Fluid extraction performance comparison based on mean dice coefficient on different oct imagery.

Machines	CNN-STGS	[29]	[31]	[32]	[34]
Spectralis	0.647[a] 0.7859[c]	0.53[a]	0.61[a]	0.729[d]	0.77[c]
Topcon 3-D OCT 2000 Series	0.906[b]	–	–	–	–

[a] The mean Dice coefficient is computed on Duke Dataset-II [29] against all fluid markings.
[b] The mean Dice coefficient is computed on AFIO dataset [43] against all fluid markings.
[c] The mean Dice coefficient is computed on Duke Dataset-II with fluid markings of clinician 1, and.
[d] The mean Dice coefficient is computed on their own local dataset.

The sensitivity ratings in Table 8 correspond to the number of cyst fluid segments that are correctly characterized out of 704 cyst-filled B-scans, and the specificity ratings correspond to the number of serous fluid segments that are correctly identified out of 576 serous-filled B-scans. CNN-STGS has achieved 5.14% better results than [33] for extracting retinal fluid. However, this comparison is indirect as the datasets on which these performances were recorded are different. Apart from this, the overall fluid extraction ratings of CNN-STGS and the other published work using different OCT machines are presented in Table 9. The empty spaces indicate that the stats for the underlying machine were not presented.

Furthermore, the robustness of CNN-STGS for segmenting retinal layers and fluid pathology is shown in Fig. 7, along with the comparison with the manual annotations. It can be seen from Fig. 7 that CNN-STGS is able to extract retinal layers with high-level precision and accuracy regardless of the scan quality. Also, CNN-STGS is able to pick small layer changes that were missed even in the manual annotations as evident in Fig. 7 (c) and (i).

Unfortunately, Duke Dataset-III [28] does not contain manual annotations for quantitative analysis. Therefore, in this paper, we have only presented the visual results on Duke Dataset-III. Fig. 8 shows B-scans having different retinal complications, where it is evident that CNN-STGS is extremely robust in extracting retinal information from the scans regardless of the retinal pathological conditions that they depict or their acquisition machinery.

Apart from this, CNN-STGS can reconstruct nine retinal surfaces for the 3-D presentation of the human retina and the tenth surface, which represents the thickness morphology of the macular region as shown in Fig. 6. The nine retinal surfaces are merged to depict the true and

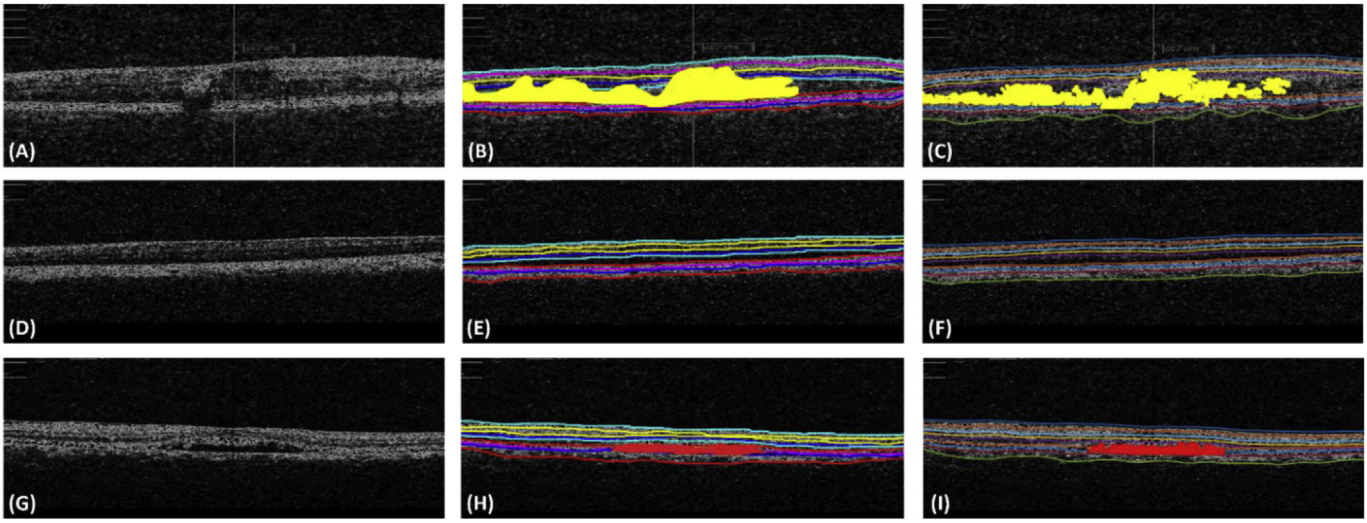

Fig. 7. Retinal layer segmentation framework: (A) ME-affected OCT scan, (B) layers and cyst ground truth superimposed on (A), (C) layers and cyst extracted by CNN-STGS from (A), (D) normal OCT scan, (E) layers and cyst ground truth superimposed on (D), (F) layers and cyst extracted by CNN-STGS from (D), (G) CSR-affected OCT scan, (H) layers and serous ground truth superimposed on (G), and (I) layers and serous extracted by CNN-STGS from (G).

objective pathological conditions of the human retina. Moreover, the visual representation of extracted fluids, along with the manual markings, is shown in Fig. 9, where it can be observed that CNN-STGS is able to accurately extract the fluid-filled regions.

Table 10 shows the time comparison of CNN-STGS with the state-of-the-art solutions, where it can be observed that CNN-STGS is among the fastest frameworks for the automated retinal image analysis.

CNN-STGS can extract complete retinal information from each B-scan in around 1.2 seconds on average on a machine with fifth-generation Intel i5 processor, 8 GB RAM, and NVIDIA GeForce 830M. Although the method proposed in Ref. [34] has the best time performance, it was only tested on Duke Dataset-II, whereas the proposed CNN-STGS has been tested on four publicly available datasets, which are acquired through different OCT machines. That makes CNN-STGS a vendor-independent framework for the analysis of retinal pathology. Furthermore, CNN-STGS utilizes a degree of coherency for the extraction of retinal layers and trained CNN models for the extraction and identification of retinal fluids. CNN-STGS also outperforms the method proposed in Ref. [34] in terms of extracting and identifying retinal fluids. To the best of our knowledge, the method proposed in Ref. [34] can only extract retinal fluids, but it cannot identify their types, whereas CNN-STGS not only extracts retinal fluids 1.59% better than [34] (in terms of Dice coefficient), but it can also identify the retinal fluid type. That makes CNN-STGS a significant improvement over [34]. Moreover, the training of the AlexNet-based RCNN model was conducted with 20 epochs, batch size of 32 having an initial learning rate of 1^{-6}, and the training of the second-stage CNN model was conducted with 10 epochs, batch size of 5 and 600 iterations having an initial learning rate of 10^{-4} on the subset of scans from all the datasets in Table 2. Both models have been trained on 4992 OCT B-scans.

5. Discussion

A deep structure tensor graph search-based segmentation framework (CNN-STGS) has been proposed here for the extraction of nine retinal layers, along with the extraction and identification of cyst and serous fluids. The extracted layer information is further utilized by CNN-STGS for the 3-D presentation of retinal surfaces as well as the 3-D retina. The uniqueness in the proposed framework is that it can extract retinal information from OCT B-scans irrespective of their quality, their acquisition machinery, or the pathology that they present. To our best knowledge, CNN-STGS is unique and tested on four different publicly available OCT datasets acquired through different OCT machines. Apart from this, the proposed segmentation framework has been extensively compared with the state-of-the-art solutions, where it outperformed them for extracting retinal layers and fluid segments. CNN-STGS achieved 1.98 μm, 0.09 μm, 0.02 μm, and 0.12 μm improvements over [34] in extracting RNFL, GCL-IPL, OPL, and ONL-ISM, respectively, whereas CNN-STGS achieved 0.46 μm, 0.77 μm, 1.66 μm, 1.83 μm, 2.24 μm, 0.74 μm, and 0.65 μm improvements over [29] in extracting RNFL, GCL-IPL, INL, OPL, ONL-ISM, ISE, and OS-RPE, respectively, and CNN-STGS achieved 22.58 μm, 7.83 μm, 3.67 μm, 1.98 μm, 14.94 μm, 0.39 μm, and 0.55 μm improvements over [23] in extracting RNFL, GCL-IPL, INL, OPL, ONL-ISM, ISE, and OS-RPE, respectively. This is significant especially considering the fact that CNN-STGS can extract and analyze retinal information from OCT images acquired through different OCT machinery, whereas the method proposed in Refs. [23,29], and [34] was only tested on Duke Dataset-II. Furthermore, CNN-STGS achieved the 11.7%, 3.7%, and 1.59% improvements over [29,31], and [34] in terms of Dice coefficient. The CNN models employed in the proposed framework were trained on 4992 OCT scans, which are taken from all four datasets. The total training epochs of the AlexNet model and the AlexNet-based RCNN model are 10 and 20, respectively, where the stochastic gradient descent (SGD) function is used for optimization in each epoch, and two dropout layers are used in each CNN model for regularization. The detailed hyperparameter list of employed CNN is given in Table 3. Apart from this, CNN-STGS is invariant to scan quality as shown in Fig. 8. To our best knowledge, all the published methods have limitations on the scan quality and are subjective to the retinal pathology, whereas the proposed CNN-STGS can extract retinal information irrespective of both the scan quality and the retinal pathology. The time performance of CNN-STGS is around 1.2 seconds on average for extracting retinal information from each B-scan, and it is among the fastest frameworks as shown in Table 10.

6. Conclusion

This paper proposes a CNN-STGS framework that can extract nine retinal layers with the robust identification of retinal fluids and the 3-D presentation of the human retina. To our best knowledge, CNN-STGS is one of the unique frameworks that gives a complete 3-D analysis of retinal morphology irrespective of acquisition machinery. Furthermore, CNN-STGS has been tested on 46,541 retinal SD-OCT scans. The performance of CNN-STGS for the extraction of retinal information is

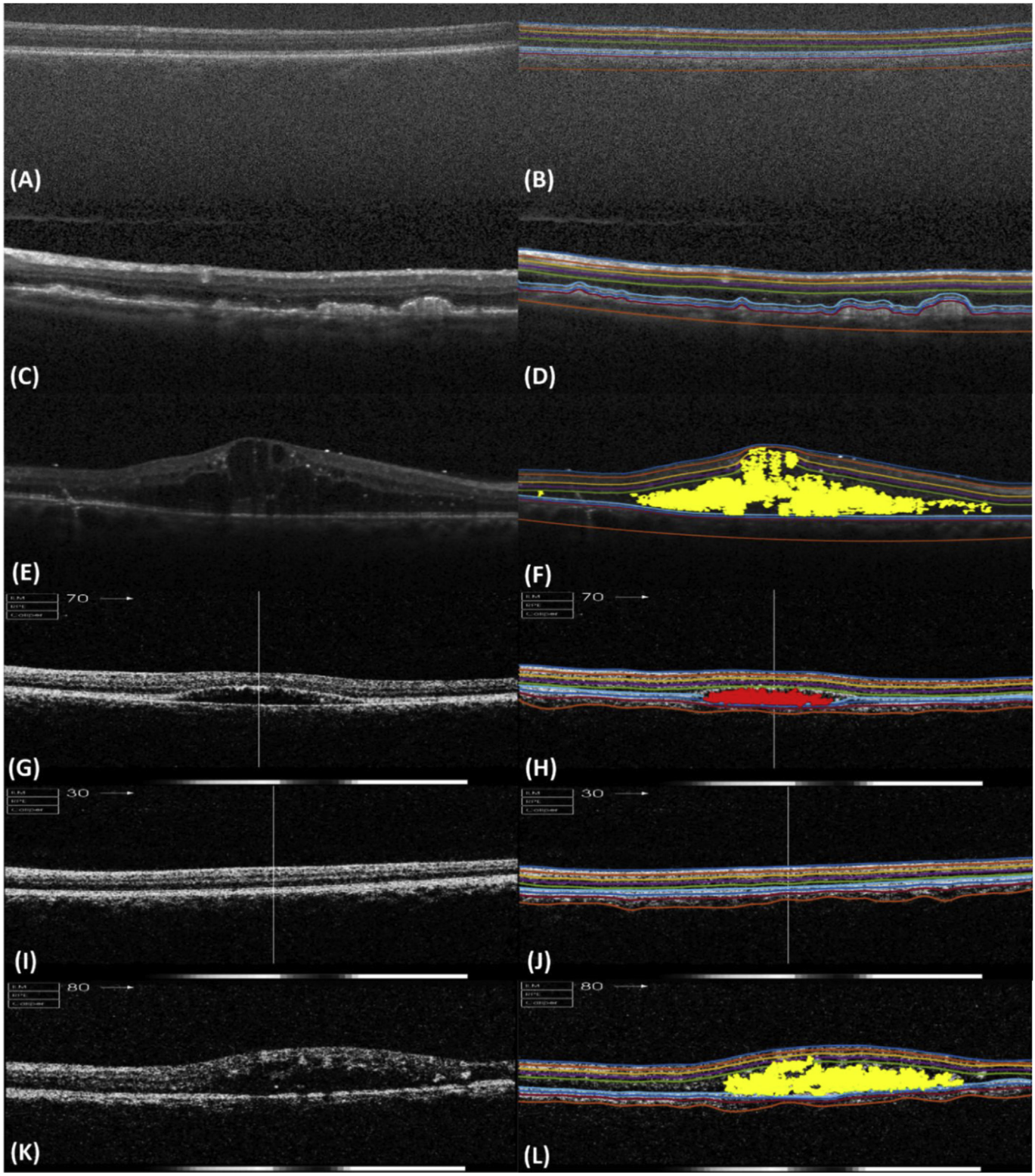

Fig. 8. Extracted layers, along with fluid pathology, through the proposed CNN-STGS framework: (A) original healthy scans from Ref. [38], (B) result of CNN-STGS on (A), (C) original AMD-affected scan from Ref. [28], (D) result of CNN-STGS on (C), (E) DME-affected scans from Ref. [29], (F) result of CNN-STGS on (E) (cyst fluid is highlighted in yellow), (G) CSR-affected scans from AFIO dataset [43], (H) result of CNN-STGS on (G) (serous fluid is highlighted in red), (I) healthy scan from AFIO dataset [43], (J) result of CNN-STGS on (I), (K) ME-affected scans from AFIO dataset [43], and (L) result of CNN-STGS on (K).

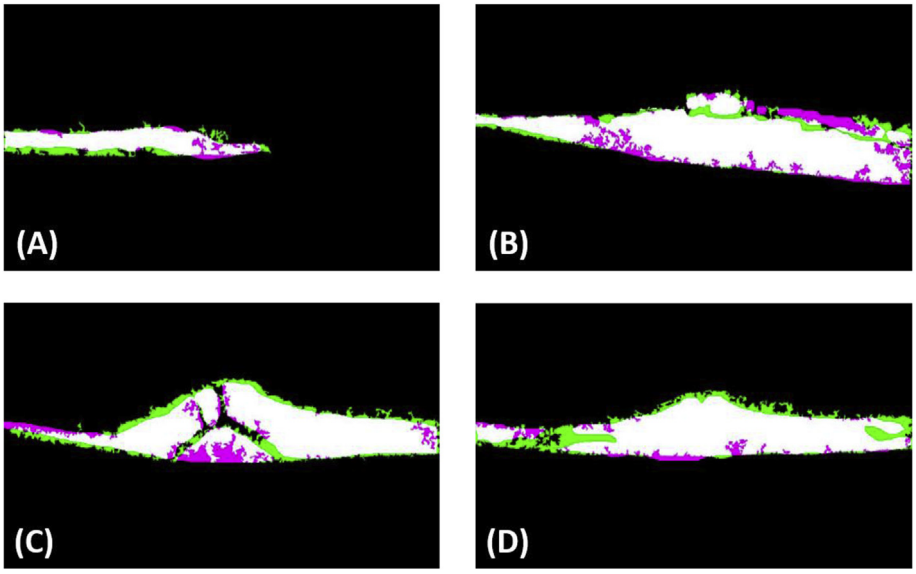

Fig. 9. CNN-STGS fluid extraction against manual markings: (A) serous fluid, (B)–(D) cyst fluid. Pink represents the manual markings, green represents the fluid extracted through CNN-STGS, and white represents the overlapped area.

Table 10
Time comparison of cnn-stgs with the state-of-the-art framework.

Metric	CNN-STGS	[23]	[29]	[30]	[31]	[32]	[33]	[34]	Manual [29]
Per B-scan on average	1.2 seconds	1.8 seconds	11.4 seconds	43.1 seconds	29.25 seconds	13.2 seconds	30 seconds per volume	0.01 seconds	5.5 minutes

highly remarkable as compared with the existing solutions as discussed in section 4. Furthermore, CNN-STGS achieved the mean Dice coefficient of 0.906 for extracting retinal fluids, along with the overall accuracy of 98.75% for characterizing retinal fluids as a cyst or serous. The cumulative training time for the incorporated CNN models is around one minute on average, which is extremely efficient.

Conflicts of interest

None declared.

Acknowledgment

This work is funded by Ignite National Technology Fund, Government of Pakistan. Grant Number: ICTRDF/TR&D/2015/08.

References

[1] Implant Gives Rats Sixth Sense for Infrared Light, Wired UK, 2013, Accessed date: 14 February 2013.
[2] R. Snell, M. Lemp, Clinical Anatomy of the Eye, second ed., (2013).
[3] G. Comers, Cystoid Macular Edema, Kellog Eye Center (Accessed June 2016).
[4] P. J. Saine, Fundus Photography: What is a Fundus Camera? Ophthalmic Photographers Society (Accessed 30 May 2016).
[5] J. Schuman, "Introduction to Optical Coherence Tomography Technology.".
[6] M. Wang, I.C. Munch, P.W. Hasler, C. Prünte, M. Larsen, Central serous chorioretinopathy, Acta Ophthalmol. 86 (2) (2008) 126–145.
[7] W. Zhang, K. Yamamoto, S. Hori, Optical coherence tomography for assessment of diabetic macular edema, Int. J. Opthalmol. 1 (2008).
[8] N. Maharjan, A. Shrestha, R. Thapa, G. Poudyal, Optical coherence tomographic assessment of macular thickness and morphological patterns in diabetic macular edema: prognosis after modified grid photocoagulation, Nepal. J. Ophthalmol. 4 (7) (2012) 128–133.
[9] N.F. Mokwa, T. Ristau, P.A. Keane, B. Kirchhoff, S.R. Sadda, S. Liakopoulos, Grading of age-related macular degeneration: comparison between color fundus photography, fluorescein angiography, and spectral domain optical coherence tomography, J. Ophthalmol. 2013 (2013) 6 85915.
[10] R.Z. Hannouche, M.P. Ávila, Detection of diabetic foveal edema with bio microscopy, fluorescein angiography and optical coherence tomography, Arq. Bras. Oftalmol. 71 (5) (2008) 759–763.
[11] D. Koleva-Georgieva, Optical Coherence Tomography Findings in Diabetic Macular Edema, (2012).
[12] Y.M. Helmy, H.R. Atta Allah, Optical coherence tomography classification of diabetic cystoid macular edema, Clin. Ophthalmol. (2013).
[13] G. Virgili, F. Menchini, V. Murro, E. Peluso, F. Rosa, G. Casazza, Optical coherence tomography (OCT) for detection of macular oedema in patients with diabetic retinopathy, Cochrane Database Syst. Rev. 7 (2011) CD008081, , https://doi.org/10.1002/14651858.
[14] B.L. Sikorski, G. Malukiewicz, J. Stafiej, H. Lesiewska-Junk, D. Raczynska, The diagnostic function of OCT in diabetic maculopathy, Mediat. Inflamm. 2013 (2013) 43456012.
[15] G. Trichonas, P.K. Kaiser, Optical coherence tomography imaging of macular oedema, Br. J. Ophthalmol. 98 (2014) ii24–ii29, https://doi.org/10.1136/bjophthalmol-2014-305305.
[16] M.R. Hee, C.A. Puliafito, J.S. Duker, E. Reichel, J.G. Coker, J.R. Wilkins, J.S. Schuman, E.A. Swanson, J, G. Fujimoto, Topography of diabetic macular edema with optical coherence tomography, Elsevier J. Ophthalmol. (2005), https://doi.org/10.1016/S0161-6420(98)93601-6.
[17] A. Martidis, J.S. Duker, P.B. Greenberg, A.H. Rogers, C.A. Puliafito, E. Reichel, C. Baumal, Intravitreal triamcinolone for refractory diabetic macular edema, Elsevier J. Ophthalmol. (2002), https://doi.org/10.1016/S0161-6420(02)00975-2.
[18] L. Zhang, W. Zhu, F. Shi, H. Chen, X. Chen, Automated segmentation of intra-retinal cystoid macular edema for retinal 3D OCT images with macular hole, Int. Symp. Biomed. Imag. 12 (2015) 1494–1497.
[19] G.R. Wilkins, O.M. Houghton, A.L. Oldenburg, Automated segmentation of intraretinal cystoid fluid in optical coherence tomography, IEEE Trans. Biomed. Eng. 59 (4) (2012) 1109–1114.
[20] J. Sugruk, S. Kiattisin, A.L. Lasantitham, Automated classification between age-related macular degeneration and diabetic macular edema in OCT image using image segmentation, IEEE Biomed. Eng. Int. Conf. 2014.
[21] B. Hassan, G. Raja, Fully automated assessment of macular edema using optical coherence tomography (OCT) images, Int. Conf. on Intell. Syst. Eng. (ICISE), 2016.
[22] D.C. Fernández, H.M. Salinas, C.A. Puliafito, Automated detection of retinal layer structures on optical coherence tomography images, Opt. Express 13 (25) (2005) 10200–10216.
[23] S.J. Chiu, X.T. Li, P. Nicholas, C.A. Toth, J.A. Izatt, S. Farsiu, Automatic segmentation of seven retinal layers in SD-OCT images congruent with expert manual segmentation, Opt. Express 18 (18) (2010) 19413–19428.
[24] Q. Yang, C.A. Reisman, Z. Wang, Y. Fukuma, M. Hangai, N. Yoshimura, A. Tomidokoro, M. Araie, A.S. Raza, D.C. Hood, K. Chan, Automated layer segmentation of macular OCT images using dual-scale gradient information, Opt. Express 18 (20) (2010) 21293–21307.
[25] A.M. Abhishek, T.T. Berendschot, S.V. Rao, S. Dabir, Segmentation and analysis of retinal layers (ILM & RPE) in optical coherence tomography images with edema, IEEE Conf. Biomed. Eng. and Sci. (IECBES) (2014) 204–209.

[26] D. Kaba, Y. Wang, C. Wang, X. Liu, H. Zhu, A.G. Salazar-Gonzalez, Y. Li, Retina layer segmentation using kernel graph cuts and continuous max-flow, Opt. Express 23 (6) (2015) 7366–7384.
[27] Y. Huang, R.P. Danis, J.W. Pak, S. Luo, J. White, X. Zhang, A. Narkar, A. Domalpally, Development of a semi-automatic segmentation method for retinal OCT images tested in patients with diabetic macular edema, PLoS One 8 (12) (2013) e82922.
[28] P.P. Srinivasan, L.A. Kim, P.S. Mettu, S.W. Cousins, G.M. Comer, J.A. Izatt, S. Farsiu, Fully automated detection of diabetic macular edema and dry age-related macular degeneration from optical coherence tomography images, Biomed. Opt. Express 5 (10) (2014), https://doi.org/10.1364/BOE.5.0035 68.
[29] S.J. Chiu, M.J. Allingham, P.S. Mettu, S.W. Cousins, J.A. Izatt, S. Farsiu, Kernel regression based segmentation of optical coherence tomography images with diabetic macular edema, Biomed. Opt. Express 6 (4) (2015).
[30] L. Fang, D. Cunefare, C. Wang, R.H. Guymer, S. Li, S. Farsiu, Automatic segmentation of nine retinal layer boundaries in OCT images of non-exudative AMD patients using deep learning and graph search, Biomed. Opt. Express 8 (5) (2017).
[31] A. Rashno, D.D. Koozekanani, P.M. Drayna, B. Nazari, S. Sadri, H. Rabbani, K.K. Parhi, Fully-automated segmentation of fluid/cyst regions in optical coherence tomography images with diabetic macular edema using neutrosophic sets and graph algorithms, IEEE Trans. Biomed. Eng. (2017) 99.
[32] C.S. Lee, A.J. Tyring, N.P. Deruyter, Y. Wu, A. Rokem, A.Y. Lee, Deep-learning based, automated segmentation of macular edema in optical coherence tomography, Biomed. Opt. Express 8 (7) (2017).
[33] T. Schlegl, S.M. Waldstein, H. Bogunovic, F. Endstraßer, A. Sadeghipour, A. Philip, D. Podkowinski, B.S. Gerendas, G. Langs, U. Schmidt-Erfurth, Fully automated detection and quantification of macular fluid in OCT using deep learning, Elsevier Ophthalmol. J. 125 (4) (2018).
[34] A.G. Roy, S. Conjeti, S.P.K. Karri, D. Sheet, A. Katouzian, C. Wachinger, N. Navab, ReLayNet: retinal layer and fluid segmentation of macular optical coherence tomography using fully convolutional networks, Biomed. Opt. Express 8 (8) (2017).
[35] T. Hassan, M.U. Akram, B. Hassan, A.M. Syed, S.A. Bazaz, Automated segmentation of subretinal layers for the detection of macular edema, Appl. Opt. 55 (2016) 454–461.
[36] B. Hassan, G. Raja, T. Hassan, M.U. Akram, Structure tensor based automated detection of macular edema and central serous retinopathy using optical coherence tomography images, J. Opt. Soc. Am. A 33 (2016) 455–463.
[37] A.M. Syed, T. Hassan, M.U. Akram, S. Naz, S. Khalid, Automated diagnosis of macular edema and central serous retinopathy through robust reconstruction of 3D retinal surfaces, Comput. Methods Progr. Biomed. 137 (2016) 1–10.
[38] S. Farsiu, S.J. Chiu, R.V. O'Connell, F.A. Folgar, E. Yuan, J.A. Izatt, C.A. Toth, Quantitative classification of eyes with and without intermediate age-related macular degeneration using optical coherence tomography, Ophthalmology 121 (1) (2014) 162–172.
[39] W. Forstner, E. Gulch, A fast operator for detection and precise location of distinct points, corners and centers of circular features, Proceedings of the ISPRS Workshop on Fast Processing of Photogrammetric Data, 1986, pp. 281–305.
[40] J. Bigun, Optimal Orientation Detection of Linear Symmetry, (1987).
[41] A. Krizhevsky, I. Sutskever, G.E. Hinton, ImageNet classification with deep convolutional neural networks, Adv. Neural Inf. Process. Syst. (NIPS) (2012).
[42] Y. Bengio, Practical recommendations for gradient based training of deep architectures, Neural Networks: Tricks of the Trade, Springer, 2012, pp. 437–478.
[43] T. Hassan, M.U. Akram, M.F. Masood, U. Yasin, BIOMISA retinal image database for macular and ocular syndromes, 15th Int. Conf. on Image Anal. and Recognition (ICIAR-2018), Springer LNCS, Portugal, 2018.